Available online at www.sciencedirect.com

ScienceDirect

Journal of the European Ceramic Society 26 (2006) 3343–3349

www.elsevier.com/locate/jeurceramsoc

NMR techniques: A non-destructive analysis to follow microstructural changes induced in ceramics

R. Viola [a], A. Tucci [b,*], G. Timellini [b,c], P. Fantazzini [d]

[a] University of Bologna, DICMA, Viale Risorgimento 2, 40136 Bologna, Italy
[b] Centro Ceramico Bologna, Via Martelli 26, 40138 Bologna, Italy
[c] University of Bologna, DICASM, Viale Risorgimento 2, 40136 Bologna, Italy
[d] University of Bologna, Department of Physics, V. Berti Pichat 6/2, 40127 Bologna, Italy

Received 30 July 2005; received in revised form 9 September 2005; accepted 17 September 2005
Available online 25 October 2005

Abstract

Magnetic resonance relaxation (MRR) and magnetic resonance imaging (MRI) of water ^{1}H nuclei confined in high-surface-to-volume ratio systems are important tools to investigate pore-space properties such as connected porosity and pore-size distribution in a non-destructive way. In the present work, MRR and MRI techniques were applied to study the microstructure of ceramic materials used for the production of tiles, with different compositions and fired at different temperatures, in terms of porosity distribution and pore-size distribution. Relaxation analysis of samples saturated with water gave a clear characterisation of the pore space of the materials, with high resolution power. Actually, the decay of the nuclear magnetization was turned into pore-size distribution, the relaxation rates depending on local surface-to-volume ratios. MRI has been applied to visualize in a non-destructive way internal sections of ceramics saturated with water, in order to check the spatial homogeneity. It was also possible to evaluate parameters connected to the local structure in the inside regions. The effects of different firing temperatures and compositions were distinguished. The results were compared with microstructural studies carried out by scanning electron microscopy (SEM) and mercury intrusion porosimetry (MIP). SEM analysis confirmed the outcomes of MRR and MRI, and the comparison with MIP made it clear that a higher temperature allows the formation of larger pores connected by smaller channels. MRR and MRI proved to be particularly useful to assess, in a non-destructive way, the effects of different fluxes on the final microstructures.

© 2005 Elsevier Ltd. All rights reserved.

Keywords: NMR; Non-destructive evaluation; Microstructure; Porosity; Traditional ceramics

1. Introduction

Pore-size dimensions and distributions and pore-space connectivity influence fluid transport within a porous structure. Their knowledge is a key issue in a wide class of engineering problems devoted, for example, to assess the safety of waste repositories, or to evaluate the fate and transport of underground contaminants, the spreading and dilution of chemical pollutants inside soils and sandy/silty aquifers. Moreover, pore-space characteristics and transport properties determine the possibility to pump non-aqueous phase liquid (NAPL) from contaminated aquifers. Another applicative example may be derived from core-analysis as well as from well-logging: the amount of water that cannot be produced (or the fraction that will be produced with the hydrocarbon) is an important parameter for numerical simulation of a reservoir. Only simplified geometrical representations of the pore space (e.g. a bundle of capillary tubes) can currently easily be modelled. Such pore network models can be used to predict macroscopic transport coefficients that can then be compared with experimental values. However, a fundamental understanding of how local microstructural variations can influence macroscopic transport is still lacking, and it is in this regard that nuclear magnetic resonance (NMR)[1–3] techniques have considerable potential.

The microstructure of silicatic ceramics, used for tile production, is rather heterogeneous, characterised by a glassy matrix containing crystalline phases, pores and cracks. All these material discontinuities, able to act as stress concentration and to

---

* Corresponding author. Tel.: +39 051 534015; fax: +39 051 530085.
E-mail addresses: rossella.viola@guest.ing.unibo.it (R. Viola), tucci@cencerbo.it (A. Tucci), timellini@cencerbo.it (G. Timellini), paola.fantazzini@unibo.it (P. Fantazzini).

0955-2219/$ – see front matter © 2005 Elsevier Ltd. All rights reserved.
doi:10.1016/j.jeurceramsoc.2005.09.055

become fracture origin, contribute to strongly decrease the mechanical strength of these structural products. The role played by porosity, in the performances of wall and floor ceramic tiles, is so important, that the classification of ceramic tiles for different destination is based on the water absorption value (International Standard ISO 13006, 1998). This characteristic is, however, not sufficient to give information on the real microstructure of a product, i.e. pore-size distribution or shape of pores. So it is possible that two products, belonging to the same class, as defined by the Standard for the water absorption value, have a completely different behaviour during service, for the presence of internal flaws.

Ceramic microstructure are routinely characterised by techniques such as scanning electron microscopy (SEM) and mercury intrusion porosimetry (MIP). The results depend strongly on the length scales involved. NMR relaxometry (MRR) of water ^{1}H nuclei has been introduced to investigate pore-space structure in high surface-to-volume ratio (*S*/*V*) systems in a non-invasive and non-destructive way.[3] Under specific experimental conditions, the signal amplitude is proportional to the number of nuclear spins at a given value of the magnetic field. The detection of water ^{1}H nuclei of a fluid, usually water, fully saturating a porous system allows to quantify the porosity. Moreover, structural characteristics of the pore space itself can be determined, relying on the so called “surface effects”. NMR relaxation times of confined water may be many orders of magnitude shorter than the times in bulk water, and distributions of relaxation times may be many decades wide. These effects can be related to properties of the porous medium such as local *S*/*V* ratio distributions.

In brief, let us consider an isolated “pore” saturated with water, with volume *V* and surface *S*. During an NMR experiment, the water molecule and therefore also the ^{1}H nuclei travels randomly through the pore due to Brownian motion. If the diffusion of the random walking molecules of the fluid is fast enough to maintain the nuclear magnetization nearly constant throughout the pore (fast diffusion regime), the relaxation rates and pore characteristics are related by the simple relationship $1/T_{1,2} = \rho_{1,2}\ S/V + 1/T_{1,2\text{-bulk}}$, where $1/T_1$ and $1/T_2$ are the longitudinal and transverse relaxation rates (the reciprocals of the relaxation times), respectively, and ρ is the so-called surface relaxivity. The latter represents the velocity at which the nuclear magnetization flows out at the pore wall. In real porous media, pores are not isolated, and NMR relaxation data are sums of exponentially decaying components, reflecting local *S*/*V* ratios, combined with some unavoidable measurement noise. Experimental data may be turned into “pore-size” distributions by the so-called inversion of the decay data. In this paper, the inversion analysis was performed by UPEN, a Uniform PENalty inversion algorithm for multiexponential decay data[4,5] that, instead of using a uniform smoothing coefficient, varies the coefficient along with the relaxation time so as to keep the smoothing penalty roughly uniform.

NMR imaging (MRI) of materials[2,3] is much less known than medical NMR imaging, but the progress in methodological development along with the identification of significant applications, for example, to material flow and soft matter analysis, has been leading to increasing use of the method. MRI is a non-invasive analytical technique, which is capable of producing images of arbitrarily oriented slices through optically non-transparent objects. Materials can be penetrated by radio-frequency (rf) waves, and the signal is hardly attenuated by absorption and emission of rf energy at the resonance frequencies of the nuclear spins. In this sense, the objects appear transparent to rf waves, while they are non-transparent to electromagnetic waves at optical frequencies, where the human eye is a sensitive detector, or exhibit different absorption properties as provided, for instance, by X-rays and by electron beams.

The analytical techniques, SEM and MIP, available to study ceramic microstructure are all destructive ones, so the possibility to apply NMR analysis could represent a real innovation. Preliminary studies[6,7] have shown the potential and feasibility of the combined use of MRI and MRR methods in the investigation of the structure of ceramic materials. Moreover, porosity alone does not explain structural changes and it is in this regard that NMR parameters T_1 and T_2 show considerable potential, representing the ‘fingerprint’ of the medium, as explained above.

In the present work, MRI and MRR techniques have been used, as non-destructive analysis, in order to detect the microstructure of ceramic products obtained with different compositions and at different sintering temperatures. The results obtained by MRR and MRI were combined with those from MIP and SEM on the same samples. NMR techniques confirm the presence or absence of interconnected pores at each step of the analysis and, most importantly, add useful information about the pore-size distribution and the spatial heterogeneity of the ceramic samples.

2. Experimental details

2.1. Magnetic resonance analyses

Nuclear magnetic resonance exploits the interaction of the nuclei of a sample with magnetic fields. A magnetic field is applied to polarize the nuclear magnetic moments; time-dependent radio-frequency irradiations are used to stimulate the spectroscopic response, and magnetic field gradients are needed in order to obtain spatial resolution (imaging). More specifically, NMR denotes the rf communication between laboratory transmitters and receivers on one side and the magnetic polarization of atomic nuclei exposed to a magnetic field on the other side. After rf irradiation, the decay of the nuclear magnetization of the ^{1}H nuclei can be acquired and visualized on the screen of a computer. The frequency ω_L with which the atomic nuclei respond is called the *Larmor frequency*. It is related to the strength of the magnetic field, B_0, at the site of the nucleus by the fundamental equation $\omega_L = -\gamma B_0$, where γ is the gyromagnetic ratio of the observed nuclide.

The experimental setup is depicted in Fig. 1. It consists of a NMR spectrometer console, a magnet, high-power rf transmitters and a rf receiver. The magnet produces the B_0 field necessary for the NMR experiment. Within the magnet is the probe. The probe contains the rf coil for producing the B_1 magnetic field necessary to rotate the spins by 90° or 180° with respect to the magnetic field direction. The rf coil also detects the signal

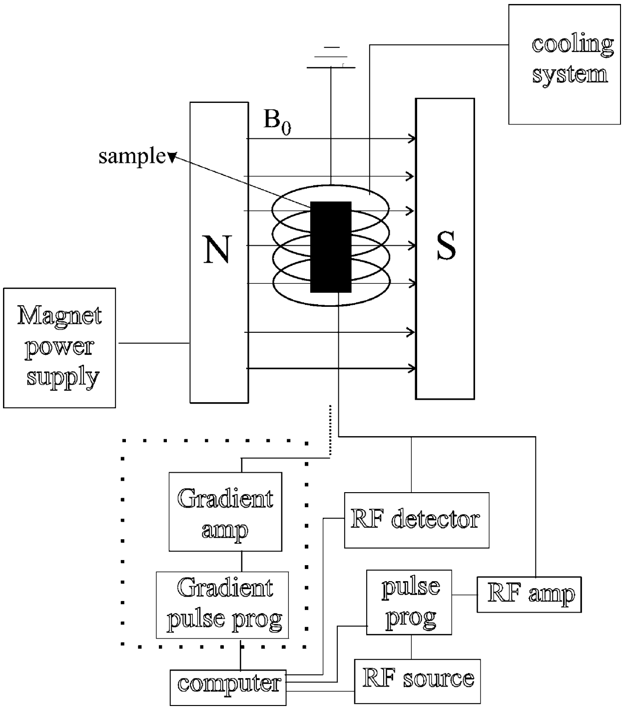

Fig. 1. Schematic representation of the major systems of a nuclear magnetic resonance spectrometer. The dashed rectangle is for imaging.

from the spins within the sample, placed within the rf coil of the probe. For imaging a set of gradient coils is added, that produce B_0 gradients along x-, y-, and z-axes. A computer controls the sequence of events (pulse programmer) for rf and gradients during the experiment, and is used for data acquisition, evaluation and display.

2.2. Samples and experimental

A standard industrial body mix for porcelain stoneware tiles, labelled A, containing 45% of kaolinitic and illitic clays, 31% of sodium and potassium feldspars and 26% of sand, was used as reference material. In order to change the microstructure, 5% of the original fluxing agent, a sodium feldspar, was replaced with another flux, a crushed soda-lime glass, having two different grain size distributions, a fine and a coarse one. The corresponding samples were labelled B and C. In Table 1, the particle size distribution, determined using a laser particle size analyser (MASTER-SIZE 2000, Malvern, UK), is reported. For the coarse grained glass, it was possible to analyse in this way only the fraction <80 μm, corresponding to 24.5%. The grain size distribution of the remaining fraction, >80 μm, assessed by using different sieves, was of 12.6% in the range 80–125 μm, of 18.0% in the range 125–250 μm, of 13.6% in the range 250–500 μm, and of 31.4% over 500 μm.

Table 1
Particle size distribution of the flux used

	d_{10} (μm)	d_{50} (μm)	d_{90} (μm)
Coarse[a]	21.1	60.1	113.2
Fine	3.7	21.6	56.4

[a] Determined for the fraction <80 μm.

Table 2
Chemical analysis of the tested mixes

	A (wt.%)	B and C (wt.%)
P.F.	3.19	3.14
SiO_2	73.01	73.19
Al_2O_3	16.84	16.04
TiO_2	0.45	0.45
Fe_2O_3	0.51	0.51
CaO	0.62	1.09
MgO	0.26	0.36
K_2O	1.67	1.70
Na_2O	3.45	3.51

Table 2 shows the chemical compositions, determined by inductively coupled plasma emission spectroscopy (ICP-OES Optima 3200 XL, Perkin-Elmer, USA), of the reference material, A, and of the modified ones, B and C.

The raw materials were wet milled in a laboratory milling jar for 1 h, by using slips with 33 wt.% of water content. The slips were oven dried at 105 °C for 24 h and the dried cakes were crushed and then sieved through a 125 μm screen to obtain suitable powders for pressing. The test specimens, in the form of discs, were prepared by adding 6 wt.% of water to the sieved powders and pressed at 52 MPa by an uniaxial laboratory press. The samples were sintered in a laboratory gradient furnace, at two different temperatures, 1140 and 1160 °C, for 40 min (soaking time).

The microstructures of the fired samples were analysed by using a scanning electron microscope (JEOL T330, Japan) and a mercury intrusion porosimer (Porosimeter 2000, Fisons).

NMR measurements were performed on the fired specimens. For imaging, specimens in form of cylinders of about 40 mm diameter and 6 mm height were used, whereas for relaxometry smaller specimens, drilled from the larger previous ones were tested, 6 mm height and 7 mm diameter.

For each specimen, porosity and water absorption were determined. For porosity measurements, samples were dried in air to constant weight at 105 °C, weighed, pumped for 24 h at 10^{-3} mbar to remove air, saturated with water under vacuum, and then weighed again. Porosity (Φ), defined as pore volume/total volume, was calculated by mass differences and sample volume. Water absorption (WA) defined as mass of water/dry mass, was calculated by mass difference and dry mass.

MRI measurements were performed by means of ARTOSCAN (Esaote SPA, Genova, Italy), a tomograph consisting of a 0.2 T permanent magnet (15 mT/m maximum gradient intensity) corresponding to 8 MHz for ^{1}H. ^{1}H longitudinal and transverse relaxation curves were obtained at 25 °C and 20 MHz by a home-built relaxometer equipped with a SPINMASTER console (Stelar, Mede, PV).

3. Results and discussion

In Table 3, the values of porosity, Φ, and water absorption, WA, for the samples fired at the two temperatures, 1140 and

Table 3
Porosity (Φ) and water absorption (WA) of the samples used for MRI analysis

Sample	T (°C)	Φ (%)	WA (%)
A1	1140	18.4	8.7
A2	1160	13.5	6.1
B1	1140	8.8	3.8
B2	1160	1.1	0.5
C1	1140	16.1	7.4
C2	1160	9.4	4.1

Table 4
Porosity (Φ) and water absorption (WA) of the samples used for MRR analysis, cored from the disks used for MRI

Sample	T (°C)	Φ (%)	WA (%)
A1′	1140	18.3	8.8
A2′	1160	15.1	7.2
B1′-a	1140	6.9	2.9
B1′-b	1140	11.8	5.3
B2′-a	1160	0.1	0.02
B2′-b	1160	3.7	1.6
C1′	1140	13.8	6.5
C2′	1160	8.7	4.1

1160 °C, are reported. The increase in temperature always causes a decrease of both Φ and WA, more evident for B samples. It is evident that B samples have lower Φ and WA values than A and C.

The same samples were used for MRI analysis and the results are reported in Fig. 2a and b, showing the sections corresponding to the maximum diameter of the ceramic disks, close to one another, acquired at the same time. The images point out as samples A1, A2 and C1, C2 are homogeneously saturated with water, whereas B1 and B2 appear very inhomogeneous. In order to verify this spatial heterogeneity for the B samples, measurements have been repeated by turning the samples shown in Fig. 2a upside down. The image obtained, reported in Fig. 2b, makes us confident that the phenomenon is real and not due to instrumental artifacts. The signal intensity in each set (A, B, and C) has a trend opposite to the porosity, i.e. the specimens fired at higher temperature (A2, B2, and C2) have lower porosity, but higher signal. This effect is particularly evident in sample B. The explanation of this apparent contradiction, in terms of more visible signal in samples with lower porosity, may be the following. It is known[3,7] that water inside pores exhibits relaxation times that are shorter for smaller pore sizes, i.e. signal from smaller pores decays faster than from larger ones. As the signal is acquired at a fixed time (namely echo time TE, in our case TE = 10 ms), the signal detected from a large amount of water in small pores can be lower than that from a lower amount in larger ones. Therefore, the contradiction can be overcome if those samples with higher porosity—which show less signal—have pores of smaller sizes, i.e. if A1 and C1 (fired at 1140 °C) have smaller pores than A2 and C2 (fired at 1160 °C). Relaxation and SEM measurements will confirm this hypothesis.

For relaxation analysis, MRR, smaller specimens were drilled from the previous samples and, again, Φ and WA were determined, as shown in Table 4. Furthermore, to assess the microstructural heterogeneity of sample B, as revealed by MRI, specimens from the darker and lighter areas, respectively, labelled a and b in Fig. 2, were cored and tested. While for samples A and C the values of Φ and WA are in agreement with the same measured for the larger samples (Table 3) according to their homogeneous microstructure, the values for the sample B show large variations in agreement with the observed heterogeneity.

The signals, extrapolated to zero time to reduce the effects on them due to the different transverse relaxation times, should be directly proportional to the amount of hydrogens present in the samples investigated. It follows that the signal represents the amount of water in the sample, and, therefore, after division by the volume it should be proportional to the porosity. As a matter of fact, the plot of the signal extrapolated to zero time per unit volume of the different samples versus their porosity (Fig. 3) gives a straight line, passing through the origin, for both T_1 and T_2 measurements. The different

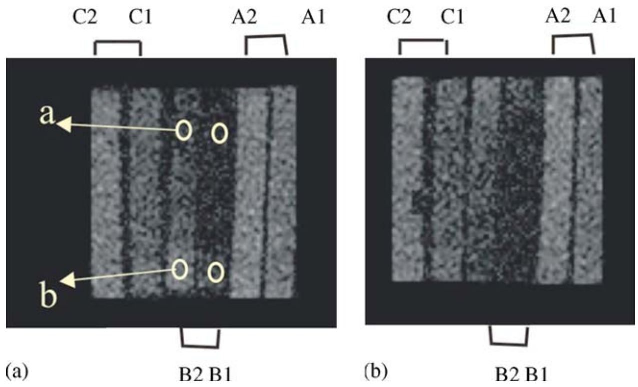

Fig. 2. Set of adjacent MRI axial sections for the samples indicated. In (b), images have been acquired after turning the samples as in (a) upside down. Each section shown is the one closest to that with the maximum diameter (voxel dimension 0.5 mm × 0.5 mm × 5 mm). Samples denoted with suffixes -a and -b were cored for MRR analysis.

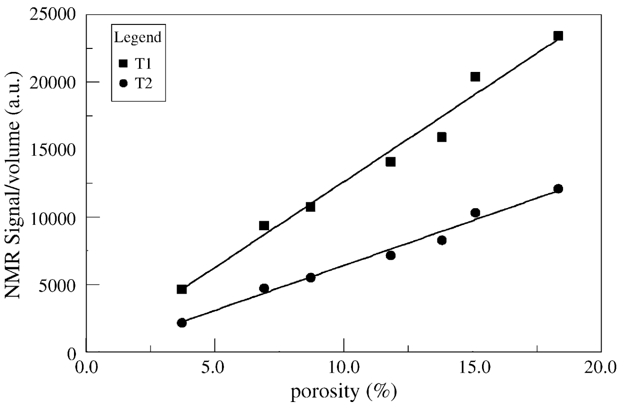

Fig. 3. Signal from NMR measurements per unit volume vs. porosity. The two sets of data refer to T_1 and T_2 measurements.

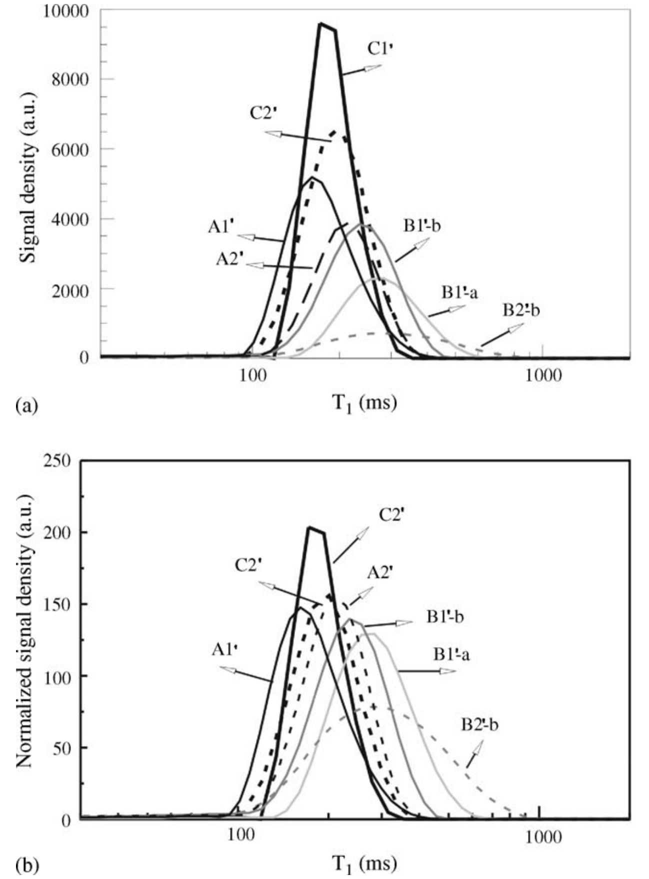

Fig. 4. Distribution of relaxation time T_1 for samples A, B, and C as indicated. (a) Signal density on *y*-axis is related to the amount of water of a chosen bin; and (b) normalized signal density is used for comparison between the samples.

slope is due to the different arbitrary units in the scale for the signal. For a new sample, the porosity can be inferred by the graph, once the relaxation measurement gives the value of the signal. Obviously, the sizes of all the samples should be comparable.

Fig. 4a and b show T_1 relaxation time distributions, related to pore-size distributions, for all the tested samples. In Fig. 4a, the areas under the curves are proportional to the signal extrapolated to zero time, whereas in Fig. 4b the normalized areas make the comparison among the distributions easier. Measurement on sample B2′-a revealed only noise, according to its low open porosity (Table 4). Samples cored from A-type and C-type disks, sintered both at 1140 and 1160 °C, show narrow distributions, indicating microstructural homogeneity, i.e. presence of pores of nearly the same dimensions. On the contrary, B-type samples show wider T_1 distributions, reflecting the presence of wider pore-size distributions. It appears clear, from Fig. 4, that, for each set of samples, the higher the temperature, i.e. the lower the porosity, the more the distributions shift toward higher relaxation times, indicating existence of larger pores, in agreement with the outcomes of MRI.

A simpler visualization of the relationship between pore-size and porosity is given in Fig. 5, where the plots of the parameters $T_{1\mathrm{gm}}$ and $T_{2\mathrm{gm}}$, calculated as $T_{i\mathrm{gm}} = \exp\langle \ln T_i \rangle$, with $i = 1$, 2, versus porosity, are reported. These average relaxation times are used to represent wide distributions, without giving excessive weight neither to shorter nor to longer relaxation times. The trends of these mean parameters, for the different sets of samples, reflect those of Fig. 4. The plots of Fig. 5 show that both T_1 and T_2 provide details of the pore space: by raising the temperature, porosity lowers and the relaxation times grow. The densification process is more efficient with higher temperatures, resulting in less interconnected porosity and in larger pores.

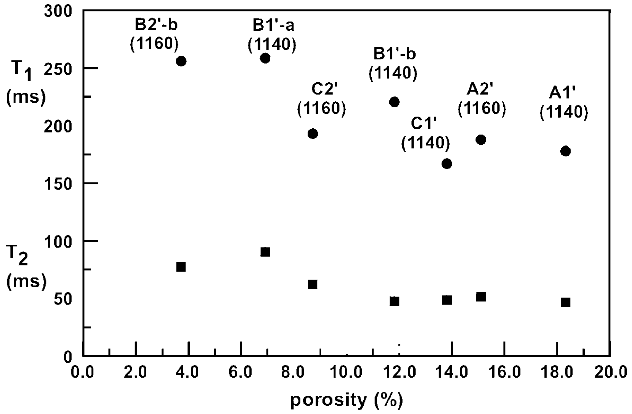

Fig. 5. T_1 (round symbols) and T_2 (square symbols) geometric mean values ($T_{1\mathrm{gm}} = \exp\langle \ln T \rangle$) as computed by the distributions obtained by UPEN vs. porosity for the samples indicated. The higher the temperature (in brackets, in °C) in each set, the lower the porosity and the higher the relaxation time.

That is confirmed by SEM analysis, performed on the same samples, undergone to the MRR analyses. As an example, the SEM images for A samples, sintered at 1140 and 1160 °C, are reported, respectively, in Fig. 6a and b. While for the sample fired at 1140 °C, only very fine pores are present (Fig. 6a), rather large pores are also clearly visible at 1160 °C (Fig. 6b). Furthermore, the SEM observations of specimens B2′-a and B2′-b (Fig. 7a and b) confirmed that B samples are strongly heterogeneous. When fired at 1160 °C, a part of it, B2′-a (Fig. 7a), is characterised by the presence of few round and close pores, embedded in a large vitrified matrix, whereas in the opposite area, B2′-b (Fig. 7b), the material is characterised by the presence of many small interconnected pores.

The microstructure revealed by the different techniques is consistent with the mechanism of sintering acting with this class of materials: the viscous flow. Once the temperature, for which the first eutectic forms, is reached, a reactive liquid phase develops, whose amount increases and viscosity decreases with the temperature. All that allows a rapid permeation of the voids among the single powder particles, leading to densification of the body. During cooling, this liquid phase forms a glassy matrix which surrounds the residual crystal phases and the newly formed ones.[8,9] Because of the high viscosity of the silica-rich liquid phase, bubbles of gas, deriving both from the decomposition of the raw materials and from the different solubility of the gases present, can remain trapped into the bulk of the material. In this way, even if a sintered sample shows

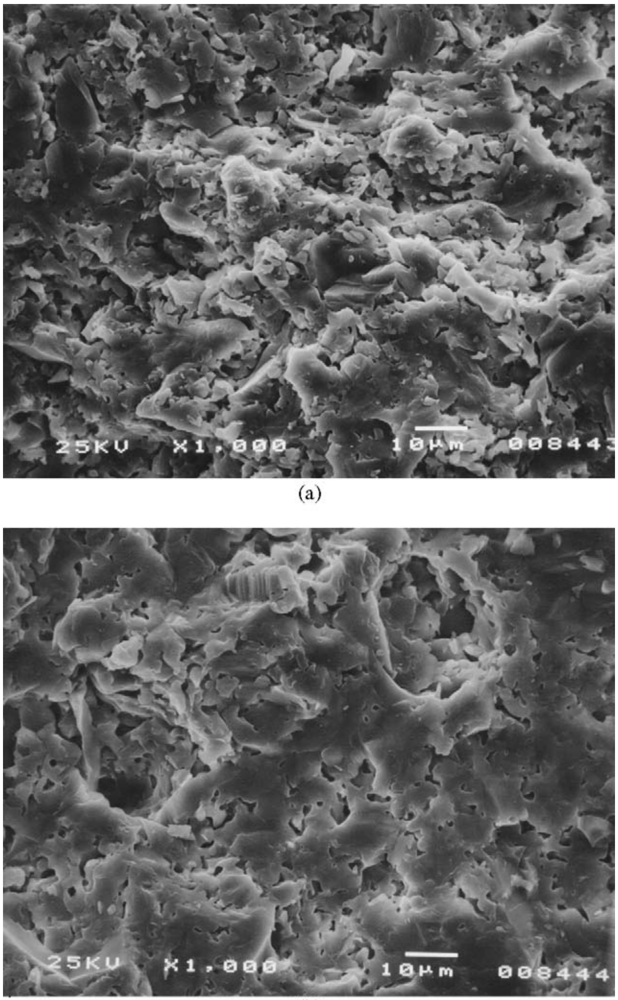

(a)

(b)

Fig. 6. SEM micrographs of the fracture surface of sample A fired at (a) 1140 °C and (b) 1160 °C.

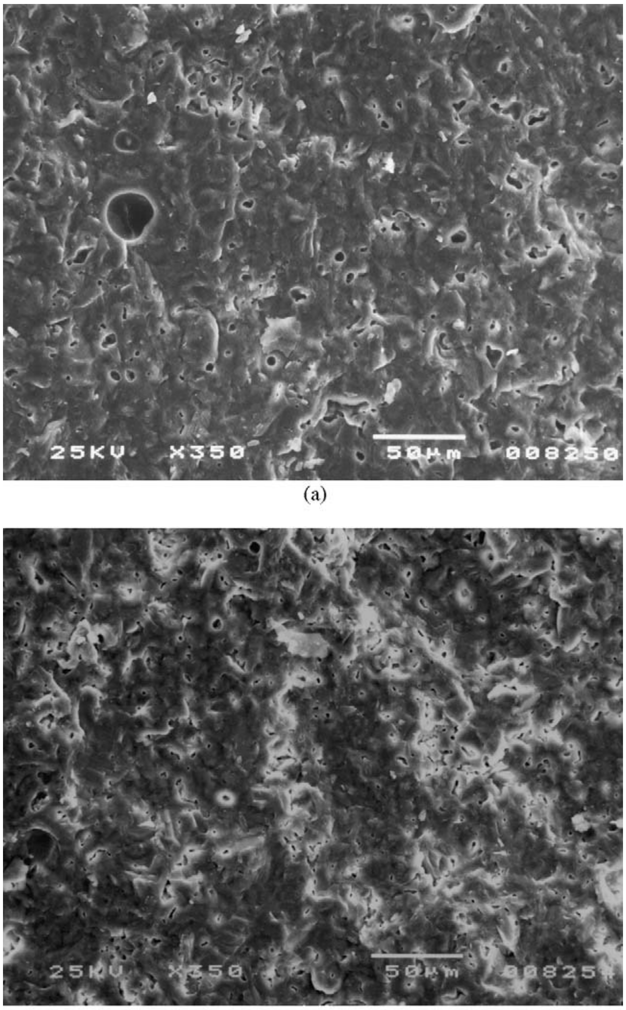

(a)

(b)

Fig. 7. SEM micrographs of the fracture surface of samples (a) B2′-a and (b) B2′-b, both fired at 1160 °C, and cored in different positions of sample B2.

very low water absorption and low NMR signal, a non-negligible amount of non-connected porosity is present in the bulk, as observed for B2′-a (Fig. 7a). The increase of temperature, besides improving the sintering rate, contributes to enlarge the pore sizes, for the coalescence of the smaller pores and the thermal expansion of the gases entrapped inside them. That explains the different morphology observed in Fig. 6a and b.

The presence of the crushed glass, with a finer grain size distribution, improves the sintering, sample B shows lower porosity than sample C, fired at the same temperature. At the same time, it decreases the thermal stability of the body during firing, so it is possible that also very minimal variation of firing temperatures are able to locally favor a higher development of viscous phases, with the consequent formation of microstructural heterogeneity. As a consequence, sample B presents a spatial variation of shrinkage degree and porosity, as detected by MRI (Fig. 2) and confirmed by SEM (Fig. 7a and b).

For all the small cores used for MRR analysis, also mercury intrusion porosimetry was performed. It is well known[7] that in relaxation measurements “size” tends to correspond to pore dimensions, whereas in MIP “size” corresponds to the dimensions of the pore “throats”, the channels connecting the pores. Fig. 8 compares the results obtained for sample B. The curves referring to the different techniques have in common the shape of the distributions. MRR and MIP distributions indicate a substantial homogeneity for samples fired at 1140 °C (B1′-a and -b). Similarly, both MRR and MIP distributions reflect heterogeneity in the sample fired at 1160 °C (B2′-b). A good agreement in the shape of the distributions (not reported) was observed also for samples A and C.

Regarding the changes of the pore size with temperature, from NMR distributions it is possible to note a shift of the peak toward higher T_1 at higher temperature, indicating larger pores. From MIP distributions, the higher temperature seems to cause the presence of many pores with small “throat” sizes. The same behaviour is shown by the samples A and C. All in all, we can say that the higher the temperature the larger the pores, connected by smaller channels.

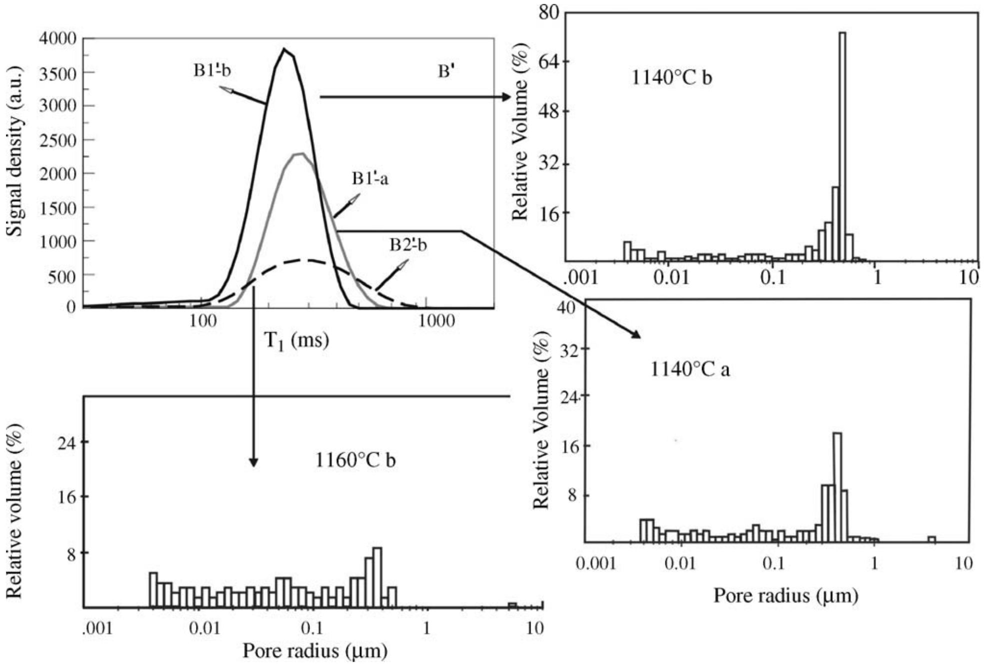

Fig. 8. Comparison between T_1 distributions and MIP distributions for sample B′. Measurements have been made on the same samples. Suffixes -a and -b refer to different positions from which they have been cored in the bigger samples used for imaging.

4. Conclusions

Starting from a standard industrial body mix used for ceramic tiles, sintered samples, with different microstructure in terms of porosity and pore-size distributions, were prepared. They were analysed with non-destructive NMR relaxation and imaging techniques. To validate these results, also traditional techniques, such as mercury intrusion porosimetry and scanning electron microscopy, were applied to the same specimens.

The results showed as NMR techniques allowed to study, in a non-destructive way, the porosity and pore-size distributions in ceramic products, in good agreement with the SEM analyses. In particular, the dramatic changes in morphology, caused by the increase of only 20° of temperature, from 1140 to 1160 °C, causing the enlargement of pore sizes, were well detected by these non-destructive techniques. At the same time, the effect of the use of different fluxing agents was proved.

The comparison with MIP made it clear as, for this class of ceramic, higher temperatures allow the formation of larger pores connected by smaller channels.

References

1. Abragam, A., *Principles of Nuclear Magnetism*. Clarendon Press, Oxford, 1986.
2. Callaghan, P. T., *Principles of Nuclear Magnetic Resonance Microscopy*. Oxford Science Publications, New York, 1991.
3. VV AA, Proceedings of the Seventh International Conference on Recent Advances in MR Applications to Porous Media, eds. Fantazzini P., Gore J. H., Korb J. -P., *Magn. Reson. Imaging*, 2005, **23**(2). For the previous MRPM Conferences see the special issues: *Magn. Reson. Imaging*, 1991, **9**, 639–888; 1994, **12**, 161–378; 1996, **14**, 697–1006; 1998, **16**, 449–714; 2001, **19**, 291–593; 2003, **21**, 159–450.
4. Borgia, G. C., Brown, R. J. S. and Fantazzini, P., Uniform-penalty inversion of multiexponential decay data. *J. Magn. Reson.*, 1998, **132**, 65–77.
5. Borgia, G. C., Brown, R. J. S. and Fantazzini, P., Uniform-penalty inversion of multiexponential decay data II: data spacing, T_2 data, systematic data errors, and diagnostics. *J. Magn. Reson.*, 2000, **147**, 273–285.
6. Borgia, G. C., Fantazzini, P., Palmonari, C. and Timellini, G., Ceramic microstructure detected by NMR relaxation and imaging of fluids in the pores. *Magn. Reson. Imaging*, 1996, **14**(7/8), 899–901.
7. Fantazzini, P., Salem, A., Timellini, G., Tucci, A. and Viola, R., Microstructure changes in fired ceramics quantified by magnetic resonance relaxation and imaging. *J. Appl. Phys.*, 2003, **79**, 7.
8. Souza, G. P., Rambaldi, E., Tucci, A., Esposito, L. and Lee, W. F., Microstructural variations in porcelain stoneware tiles as a function of flux system. *J. Am. Ceram. Soc.*, 2004, **87**(10), 1959–1966.
9. Esposito, L., Salem, A., Tucci, A., Gualtieri, A. and Jazayeri, S. H., The use of nepheline-syenite in a body mix for porcelain stoneware tiles. *J. Ceram. Int.*, 2005, **31/2**, 233–240.